Thermophysics and Aeromechanics, *2022*, *Vol. 29*, *No. 5*

DOI: 10.1134/S086986432205002X

Experimental investigation of instantaneous local flow separation in a turbulent boundary layer at various Reynolds numbers*

D.I. Zaripov[1], A.A. Lukyanov[1,2], and D.M. Markovich[1,2]

[1]*Kutateladze Institute of Thermophysics SB RAS*, *Novosibirsk*, *Russia*

[2]*Novosibirsk State University*, *Novosibirsk*, *Russia*

E-mail: zaripov.d.i@mail.ru

(*Received July 8*, *2022*; *revised July 20*, *2022*;
accepted for publications September 2, *2022*)

The effect of the Reynolds number on the mechanism of the formation of an instantaneous local flow separation that occurs in the near-wall region of a turbulent boundary layer is experimentally studied. The features of application of the high-speed planar PIV method with a high spatiotemporal resolution are discussed. Comparison of the measurement results obtained within a viscous sublayer of a turbulent boundary layer with the results of other studies showed the generality of the mechanism for the formation of an instantaneous local flow separation in the range of dynamic Reynolds number $207 \le \mathrm{Re}_\tau \le 672$.

Keywords: flow separation, turbulent boundary layer, particle image velocimetry.

Introduction

The flow separation phenomenon can have a significant impact on the efficiency and safety of a particular technique used in many spheres of human activity, such as energy, aerospace, and shipbuilding. Meanwhile, a separated turbulent flow is usually understood as the occurrence of a negative value of the mean wall shear stress. This value is the result of averaging the corresponding time signal arising from the movement of vortex structures of various nature, and the averaging result depends on the frequency of their occurrence and intensity. So, in a turbulent boundary layer, for a number of reasons, instantaneous local flow separation (ILFS) can be formed, but they will not lead to separation of the "mean" flow, but, obviously, they can affect such an integral flow quantities as hydraulic resistance. In this sense, the study of the turbulent flow structure leading to the ILFS event is of both fundamental and practical interest.

For a long time, the existence of ILFS in a zero-pressure-gradient turbulent boundary layer was considered impossible [1, 2]. However, later in a number of works [3–19], its occurrence was proved both numerically and experimentally. An analysis of publications available to date has

* The study was supported by the grant of the Russian Science Foundation No. 22-29-01274.

shown that the mechanism of ILFS occurrence and its statistical characteristics depend strongly on the Clauser parameter $\beta = (\delta^*/\tau_w)(dp/dx)$ and the dynamic Reynolds number $\mathrm{Re}_\tau = u_\tau H/\nu$, where δ^* is the displacement thickness, τ_w is the average wall shear stress, dp/dx is the longitudinal static pressure gradient, ν is the kinematic viscosity, u_τ is the dynamic velocity, and H is the channel half-width.

In [15], it was found that the probability P of ILFS formation, i.e., the time fraction of the reverse flow increases significantly with an increase in the Clauser parameter, and the mechanism of its occurrence differs for relatively small and large values of β. With an increase in the Reynolds number, the probability of ILFS formation increases sharply (P = 0.003 % at Re_τ= 90 and P = 0.0854 % at Re_τ = 1440 [3]), which can also be associated with the difference between these mechanisms at different Reynolds numbers.

It was shown in [4, 6, 12, 13, 16, 20] that the mechanism of ILFS occurrence can be associated with intense vortex structures located in the buffer region of the turbulent boundary layer. A more complete picture of the ILFSs formation was proposed in [9], according to which they are induced by near-wall transverse vortex structures formed as a result of interaction between large-scale accelerated and decelerated flow regions. However, the authors of [9] considered the flow at a relatively small value of $\mathrm{Re}_\tau \approx 200$, so the validity of the described mechanism with an increase in the Reynolds number requires additional verification.

According to [4, 13], on average, the height of the ILFS region in a zero-pressure-gradient turbulent boundary layer is approximately 5 times less than the thickness of the viscous sublayer, i.e., $\Delta y^+ = 1$, where symbol "+" denotes the quantities in wall units, i.e., scaled to the length ν/u_τ and time ν/u_τ^2. Moreover, in some cases, the spatial extent of the ILFS region can be less than the Kolmogorov length scale [9]. The value of velocity in the near-wall region of the turbulent boundary layer, including the ILFS region, is of the same order as the measurement uncertainty. This can have a significant effect on the measured spatiotemporal characteristics of the ILFS [11]. The combination of these factors demonstrates the complexity and nontriviality of the experimental study of the ILFS phenomenon and explains the false conclusions made earlier, for example, in [1, 2].

Experimental setup and experimental methods

The experiments were carried out using the high-speed planar PIV (Particle Image Velocimetry) method [21, 22], which allows one to obtain instantaneous velocity vector fields with a high spatiotemporal resolution. The measurements were made in an optically transparent test section 6 m long with a square cross section ($2H \times 2H$ = 0.1 × 0.1 m) at a distance of 5 m from the inlet. Air was used as a working medium, and a glycerol aerosol with an average particle diameter of 1 μm was used as tracer particles. To ensure uniform seeding of tracer particles over the fluid volume, a special chamber (0.6 × 0.6 × 2.4 m) was installed at the test section inlet, and to ensure a developed turbulent flow, a turbulent grid made of metal rods with a diameter of 1.4 mm in 6 mm increments was mounted there. A constant air flow in the measurement area was maintained by a set of critical nozzles installed between the compressor and the test section. The studies were carried out at two Reynolds numbers $\mathrm{Re} = U_b H/\nu$ = 6200 and 12400, where U_b is the bulk velocity.

Preliminary measurements of the profiles of the streamwise mean velocity along the test section showed that the flow in the measurement area was turbulent, symmetrical, and was already stabilized at a distance of ~ 80H (40 calibers) from the test section inlet for all considered Reynolds numbers. Therefore, the main measurements in the study of ILFS phenomenon

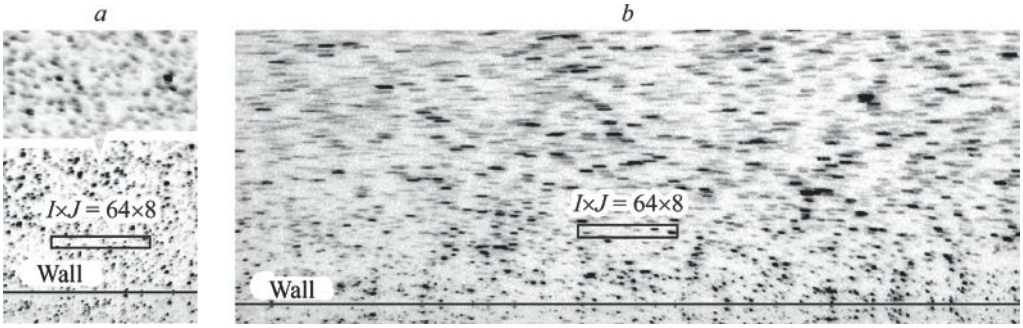

Fig. 1. Typical PIV images (inverted) obtained in a series of basic experiments at Re = 6200 (*a*) and 12400 (*b*).

were performed at a distance of 100*H* from the test section inlet. In a series of basic experiments, videos were taken at a frame rate of 4900 and 3400 Hz with a resolution of 160×1280 and 640×240 px, which allowed us to cover a flow area of 2×16 and 4.47×1.78 mm (14.3×114.1 and 63.5×23.9 in wall units) at Re = 6200 and 12400, respectively. Since the ILFS is a rather rare event, 63 and 30 video fragments were processed to detect several independent events, corresponding to the total observation time T = 257 and 221 s.

To achieve convergence of the result, 5 iterations were performed using the iterative PIV method [21]. The obtained images were processed using non-overlapping interrogation windows with the size of $I \times J = 64 \times 8$ px elongated in the streamwise direction. When choosing the interrogation window size, a compromise between the measurement uncertainty and the spatial resolution was reached. This size corresponds to $I^+ \times J^+ = 5.6 \times 0.7$ and 6.4×0.8 for Re = 6200 and 12400, respectively. The chosen spatial resolution was 2–3 times smaller than the Kolmogorov length scale λ_K in the near wall region of the turbulent boundary layer. The interrogation window closest to the wall was located at a distance of y_1= 4.5 px, which corresponds to y_1^+ = 0.4 and 0.44 for the considered values of the Reynolds number. In order to reduce the effect of measurement uncertainty, all velocity time signals were filtered according to the procedure described in [21]. It was shown in [11] that the application of this procedure allows significant reduction in the effect of measurement uncertainty and reliable estimation of integral characteristics of the ILFS region. The selected measurement parameters cover the expected range of the space-time extent of the ILFS region. The dynamic velocity used in calculation of dimensionless quantities was estimated from the profile of the mean streamwise velocity U in the viscous sublayer $u_\tau = [\nu(\partial U/\partial y)_{y=0}]^{0.5}$. In the case under consideration, u_τ = 0.107 and 0.202 m/s at Re = 6200 and 12400 (Re_τ = 357 and 672). Typical PIV images are shown in Fig. 1.

The distributions of the mean streamwise velocity and ILFS probability along the distance from the wall are shown in Fig. 2. The probability was calculated as the ratio of time during which the negative values of the streamwise velocity are observed to the total observation time. It can be seen that these distributions are in good agreement with the results of direct numerical simulation (Direct Numerical Simulation, DNS) [4, 9] and with similar experimental data obtained in [9] at Re = 3100.

Results of the study of instantaneous local flow separation

In the experiment, the ILFS event was determined from the condition $u < 0$ at the computational grid node closest to the wall. In total, 27 (Re_τ = 357) and 94 (Re_τ = 672) independent

ILFS events were detected in the experiment. The use of the high-speed PIV method allowed the analysis of a velocity change for a sufficiently long period of time. To obtain a statistical picture of the flow in the vicinity of the ILFS region, the conditional averaging procedure was used:

$$\langle \varphi \rangle = \left\langle \varphi\left(t - t_i, x - x_i, y - y_i\right)\Big|_{t=t_i,\, x=x_i,\, y=y_i} \right\rangle,$$

where φ is the streamwise or wall-normal component of the velocity vector, (t, x, y) are the time and coordinates in the measurement area, ($t - t_i$, $x - x_i$, $y - y_i$) are the time and coordinates in the new coordinate system, (t_i, x_i, y_i) are the time and coordinates of the ith ILFS event. Thus, in the new coordinate system, the ILFS regions were conditionally centered at the point with coordinates (0, 0, 0).

Conditionally averaged time signals of two velocity components in the viscous sublayer ($y^+ = 1$) of the turbulent boundary layer are presented in Fig. 3. Alternating regions of descending ($-5 < t^+ < 0$) and ascending ($0 < t^+ < 5$) flows are observed in the vicinity of $t^+ = 0$ in Fig. 3*b*. It was shown in [9] that these regions are formed due to the motion of a near-wall transverse vortex structure. According to [23], such vortex structures induce descending and ascending flows corresponding to $Q4$ ($u' > 0$, $v' < 0$) and $Q2$ ($u' < 0$, $v' > 0$) events. However, the events observed in Fig. 3 in the time range $-5 < t^+ < 5$, appear at $u' < 0$, i.e., they are classified as events $Q3$ ($u' < 0$, $v' < 0$) and $Q2$ ($u' < 0$, $v' > 0$), but not $Q4$ and $Q2$. This is explained by the fact that, on average, ILFS events occur in the tail of the large-scale region ($-50 < t^+ < 0$) of the retarded motion (see Fig. 3*a*). Moreover, the situation changes with a distance from the wall [9]. For this reason, this terminology is not used below.

Figure 3*b* demonstrates alternating regions of descending ($-5 < t^+ < 0$) and ascending ($0 < t^+ < 5$) flows in the vicinity of $t^+ = 0$, and Figure 3*a* shows the regions of decelerated ($-50 < t^+ < 0$) and accelerated ($0 < t^+ < 60$) flows. This indicates that the main mechanism

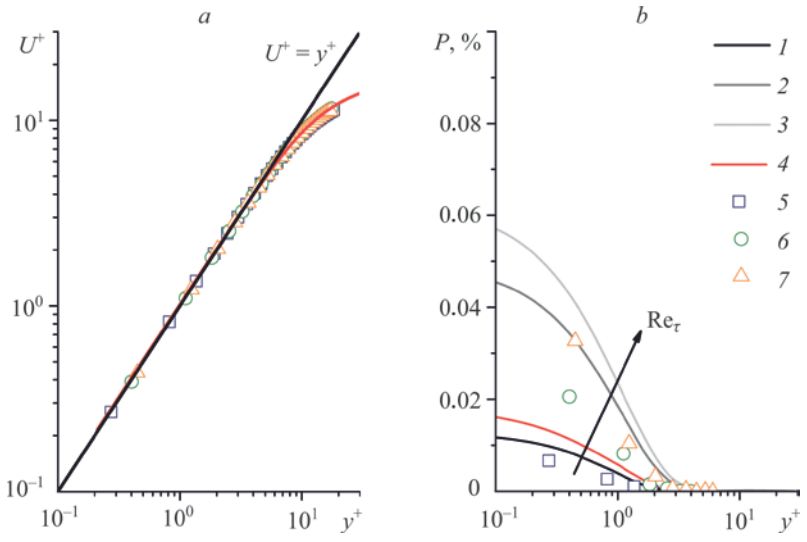

Fig. 2. Profiles of a mean streamwise velocity U^+ (*a*) and ILFS probability P (*b*). The results obtained by DNS [4] at $\mathrm{Re}_\tau = 180$ (*1*), 590 (*2*), 1000 (*3*), DNS [9] at $\mathrm{Re}_\tau = 211$ (*4*), PIV [9] at $\mathrm{Re}_\tau = 207$ (*5*), and PIV at $\mathrm{Re}_\tau = 357$ (*6*), 672 (*7*).

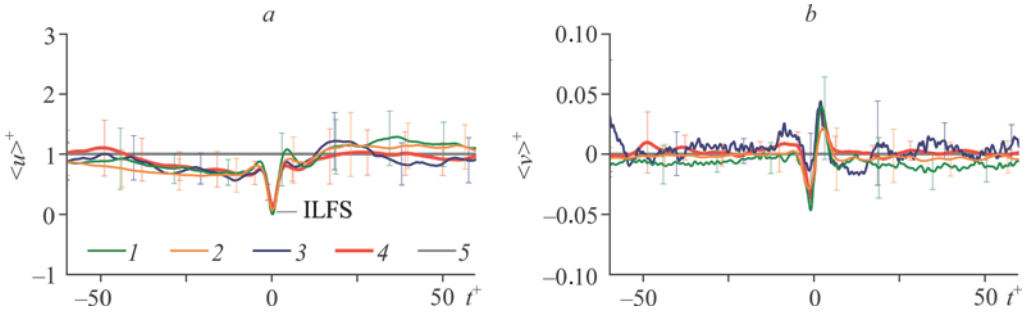

Fig. 3. Conditionally averaged signals of streamwise $<u>^+$ (*a*) and wall-normal $<v>^+$ (*b*) velocities and their standard deviations at $y^+ = 1$.
The results obtained by PIV at $\mathrm{Re}_\tau = 357$ (*1*), 672 (*2*), PIV [9] at $\mathrm{Re}_\tau = 207$ (*3*), and DNS [9] at $\mathrm{Re}_\tau = 211$ (*4*). Local mean value (*5*).

of ILFS formation is associated with the motion of the near-wall vortex structures and their interaction with large-scale flow regions.

According to [5, 20], the ILFS event can be caused by a force directed from a large-scale accelerated flow region located above the ILFS region. It was shown in [9] that such a flow region is originated upstream relative to the ILFS region. In Fig. 3*a*, this region can be determined from the overestimated $<u>^+$ value in the time period $0 < t^+ < 60$. In the spatial region, the flow pattern, observed in Fig. 3, corresponds to the interaction of two large-scale accelerated and decelerated flow regions located upstream and downstream of the ILSF region, respectively. According to the mechanism of the near-wall turbulence formation described in [24 – 27], this type of interaction leads to the formation of a strong shear layer at the interface between these regions, which develops due to the loss of this layer stability, first into near-wall transverse vortex structures, and then into a chain of horseshoe-like structures. The structures, which are the most intense and close to the wall, induce the ILFS event. Indeed, in Fig. 3*b*, we can see a trace in the form of descending and ascending flows from the moving near-wall transverse vortex structure during time period $-5 < t^+ < 5$.

The similarity between the velocity time signals obtained experimentally (PIV) at $\mathrm{Re}_\tau = 357$ and 672, with similar data obtained at $\mathrm{Re}_\tau = 207$ and 211 [9], indicates the generality of the mechanism of the ILFS formation in the range of Reynolds numbers $207 < \mathrm{Re}_\tau < 672$, i.e., in the range of a sharp increase in the ILFS probability.

Conclusion

The instantaneous local flow separation was experimentally studied at the dynamic Reynolds number $\mathrm{Re}_\tau = 357$ and 672 at the example of a developed turbulent flow in a channel with a square cross section. The experiments were carried out using the high-speed planar PIV method with a high spatiotemporal resolution. The conditionally averaged velocity time signals obtained in the viscous sublayer ($y^+ = 1$) of the turbulent boundary layer were analyzed. The found similarity between these signals and the results of other studies testifies to the generality of the mechanism of formation of instantaneous local flow separation in the range of Reynolds numbers $207 \le \mathrm{Re}_\tau \le 672$. According to this mechanism, it is induced by transverse vortex structures located in the buffer region of the turbulent boundary layer and formed as a result of interaction of large-scale accelerated and decelerated flow regions.

References

1. **H. Eckelmann,** The structure of the viscous sublayer and the adjacent wall region in a turbulent channel flow, J. Fluid Mech., 1974, Vol. 65, No. 3, P. 439–459.
2. **K.J. Colella and W.L. Keith,** Measurements and scaling of wall shear stress fluctuations, Exp. Fluids, 2003, Vol. 34, No. 2, P. 253–260.
3. **Z. Hu, C.L. Morfey, and N.D. Sandham,** Wall pressure and shear stress spectra from direct simulations of channel flow, AIAA J., 2006, Vol. 44, No. 7, P. 1541–1549.
4. **P. Lenaers, Q. Li, G. Brethouwer, P. Schlatter, and R. Örlü,** Rare backflow and extreme wall-normal velocity fluctuations in near-wall turbulence, Phys. Fluids, 2012, Vol. 24, No. 3, P. 035110-1–035110-19.
5. **R.C. Chin, J.P. Monty, M.S. Chong, and I. Marusic,** Conditionally averaged flow topology about a critical point pair in the skin friction field of pipe flows using direct numerical simulations, Phys. Rev. Fluids, 2018, Vol. 3, No. 11, P. 114607-1–114607-13.
6. **M. Bross, T. Fuchs, and C.J. Kähler,** Interaction of coherent flow structures in adverse pressure gradient turbulent boundary layers, J. Fluid Mech., 2019, Vol. 873, P. 287–321.
7. **C.E. Willert, C. Cuvier, J.M. Foucaut, J. Klinner, M. Stanislas, J.P. Laval, S. Srinath, J. Soria, O. Amili, C. Atkinson, C.J. Kähler, S. Scharnowski, R. Hain, A. Schröder, R. Geisler, J. Agocs, and A. Röse,** Experimental evidence of near-wall reverse flow events in a zero pressure gradient turbulent boundary layer, Exp. Therm. Fluid Sci., 2018, Vol. 91, P. 320–328.
8. **B. Guerrero, M.F. Lambert, and R.C. Chin,** Extreme wall shear stress events in turbulent pipe flows: spatial characteristics of coherent motions, J. Fluid Mech., 2020, Vol. 904, P. A18-1–A18-39.
9. **D. Zaripov, V. Ivashchenko, R. Mullyadzhanov, R. Li, N. Mikheev, and C.J. Kähler,** On a mechanism of near-wall reverse flow formation in a turbulent duct flow, J. Fluid Mech., 2021, Vol. 923, P. A20-1–A20-12.
10. **D. Zaripov, V. Ivashchenko, R. Mullyadzhanov, R. Li, D. Markovich, and C.J. Kähler,** Reverse flow phenomenon in duct corners at a low Reynolds number, Phys. Fluids, 2021, Vol. 33, No. 8, P. 085130-1–085130-11.
11. **D.I. Zaripov,** Problems of an experimental study of a reverse flow in the turbulent channel flow, J. Phys. Conf. Ser., 2021, Vol. 2057, No. 1, P. 012097-1–012097-5.
12. **M.S. Chong, J.P. Monty, C. Chin, and I. Marusic,** The topology of skin friction and surface vorticity fields in wall-bounded flows, J. Turbul., 2012, Vol. 13, No. 13, P. N6-1–N6-10.
13. **J.I. Cardesa, J.P. Monty, J. Soria, and M.S. Chong,** The structure and dynamics of backflow in turbulent channels, J. Fluid Mech., 2019, Vol. 880, P. R3-1–R3-11.
14. **C. Brücker,** Evidence of rare backflow and skin-friction critical points in near-wall turbulence using micropillar imaging, Phys. Fluids, 2015, Vol. 27, No. 3, P. 031705-1–031705-7.
15. **R. Vinuesa, R. Örlü, and P. Schlatter,** Characterization of backflow events over a wing section, J. Turbul., 2017, Vol. 18, No. 2, P. 170–185.
16. **C. Diaz-Daniel, S. Laizet, and J.C. Vassilicos,** Wall shear stress fluctuations: Mixed scaling and their effects on velocity fluctuations in a turbulent boundary layer, Phys. Fluids, 2017, Vol. 29, No. 5, P. 055102-1–055102-14.
17. **Y.C. Yao, W.X. Huang, and C.X. Xu,** Amplitude modulation and extreme events in turbulent channel flow, Acta Mech. Sin., 2018, Vol. 34, No. 1, P. 1–9.
18. **R. Jalalabadi and H.J. Sung,** Influence of backflow on skin friction in turbulent pipe flow, Phys. Fluids, 2018, Vol. 30, No. 6, P. 065104-1–065104-9.
19. **C. Pan and Y. Kwon,** Extremely high wall-shear stress events in a turbulent boundary layer, J. Phys. Conf. Ser., 2018, Vol. 1001, No. 1, P. 012004-1–012004-13.
20. **J.I. Cardesa, J.P. Monty, J. Soria, and M.S. Chong,** Skin-friction critical points in wall-bounded flows, J. Phys. Conf. Ser., 2014, Vol. 506, No. 1, P. 012009-1–012009-15.
21. **D. Zaripov, R. Li, and N. Dushin,** Dissipation rate estimation in the turbulent boundary layer using high-speed planar particle image velocimetry, Exp. Fluids, 2019, Vol. 60, No. 1, P. 18-1–18-16.
22. **M.P. Tokarev, D.M. Markovich, and A.V. Bilsky,** Adaptive algorithms for PIV image processing, Computation Technologies, 2007, Vol. 12, No. 3, P. 109–131.
23. **J.M. Wallace,** Quadrant analysis in turbulence research: history and evolution, Annu. Rev. Fluid Mech., 2016, Vol. 48, No. 1, P. 131–158.
24. **S.K. Robinson,** The kinematics of turbulent boundary layer structure, NASA Tech. Memo, 1991, No. 103859, P. 479.
25. **A.V. Boiko, G.R. Grek, A.V. Dovgal, and V.V. Kozlov,** Formation of Turbulence in the Near-Wall Flows, Nauka, Novosibirsk, 1999.
26. **C.R. Smith, J.D.A. Walker, A.H. Haidari, and U. Sobrun,** On the dynamics of near-wall turbulence, Philos. Trans. R. Soc., London, Ser. A Phys. Eng. Sci., 1991, Vol. 336, No. 1641, P. 131–175.
27. **R.J. Adrian, C.D. Meinhart, and C.D. Tomkins,** Vortex organization in the outer region of the turbulent boundary layer, J. Fluid Mech., 2000, Vol. 422, P. 1–54.